SPIE Proceedings Volume 5594 -- Physics and Applications of Optoelectronic Devices, pp. 110-123, Dec. 2004

Design and realization of high-power DFB lasers

H. Wenzel*, A. Klehr, M. Braun, F. Bugge, G. Erbert, J. Fricke, A. Knauer, P. Ressel, B. Sumpf, M. Weyers and G. Tränkle

Ferdinand-Braun-Institut für Höchstfrequenztechnik, Gustav-Kirchhoff-Straße 4, 12489 Berlin, Germany

ABSTRACT

The development of high-power GaAs-based ridge wave guide distributed feedback lasers is described. The lasers emit between 760 nm and 980 nm either in TM or TE polarization. Over a large current range, the lasers exhibit stable operation in a single transversal and longitudinal mode. A maximum continuous-wave output power of about 400 mW, a spectral linewidth below 1 MHz and a side mode suppression ratio greater than 50 dB have been demonstrated at room temperature. The distributed feedback is provided by first or second order gratings, formed in an InGaP/GaAsP/InGaP multilayer structure embedded into the p-AlGaAs cladding layer. Applications of such wavelength stabilized devices in non-linear frequency conversion, spectroscopy and for excitation of atomic transitions are discussed.

Keywords: Semiconductor lasers, distributed-feedback lasers, high-power lasers

1. INTRODUCTION

Single-frequency, single-spatial mode distributed feedback (DFB) and distributed Bragg reflector (DBR) lasers have important applications in communication, spectroscopy, frequency conversion, atomic clocks and Doppler laser cooling. Whereas for InP-based lasers in the 1300–1550 nm wavelength range the fabrication of integrated Bragg gratings is well-established using multi-step epitaxial techniques, it is more complicated for shorter-wavelength GaAs-based lasers. The achievement of a continuous wave (CW) output power (P) of more than 100 mW is an additional challenge. With InP-based DFB lasers emitting at 1.3 µm a CW power of 300 mW [1] and recently of 450 mW has been obtained [2]. Here, we focus on the development of GaAs-based ridge waveguide (RW) DFB lasers emitting around and below 1 µm.

In the wavelength range 750-790 nm the highest output power reported was 10 mW in [3] and 25 mW in [4]. At 980 nm, a CW power of 200 mW [5] and 400 mW [6] has been achieved. For the intermediate wavelength range, only a high-power DBR laser emitting 278 mW at 856 nm was presented [7]. However, DBR lasers suffer from periodic nonlinearities in the light-current characteristics due to longitudinal mode hopping. In contrast, DFB lasers can operate in the same longitudinal mode over a large current range which leads to linear light-current characteristics. An advantage of DBR lasers is that current is only injected into the gain section, i.e. that the DBR section acts purely passive. In DFB lasers the current flows through the Bragg grating. Hence, its fabrication, which typically necessitates a two-step epitaxy, must obey much more stringent demands.

We reported high-power RW DFB lasers in Ref. [8] and Ref. [9], where a CW power of 200 mW at 780 nm and of 300 mW at 860 nm was achieved. In this paper, new results at other wavelengths of interest and an increase of the maximum single-mode output power to almost 400 mW will be presented. These results are based on an optimized fabrication procedure as well as an accurate modeling of the complete device.

The paper is organized as follows. In Section 2, the basic structure is described and the dependence of the laser characteristics on the coupling coefficient of the Bragg grating and its phases at the facets are investigated theoretically. The fabrication process is described in Section 3. In Section 4, characteristics of lasers emitting near 763 nm, 785 nm, 852 nm, 860 nm, and 980 nm and their potential for several applications are presented. Conclusions are given in Section 5.

* mailto://wenzel@fbh-berlin.de; http://www.fbh-berlin.de

SPIE Proceedings Volume 5594 -- Physics and Applications of Optoelectronic Devices, pp. 110-123, Dec. 2004

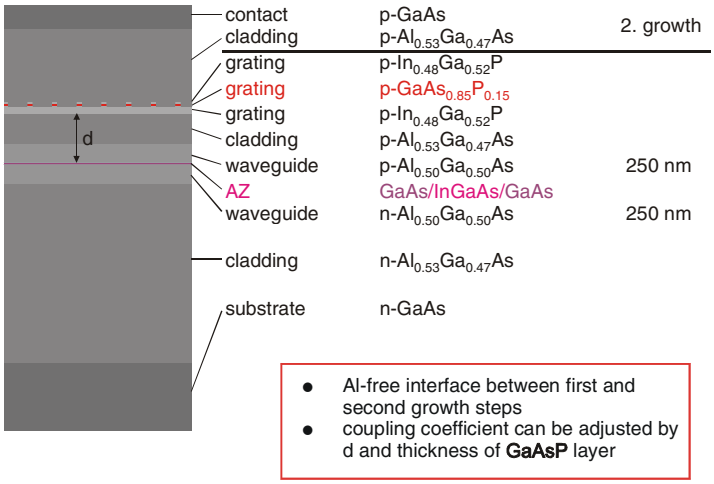

Figure 1. Transverse cross section showing epitaxial layer structure and buried Bragg grating (λ = 980 nm).

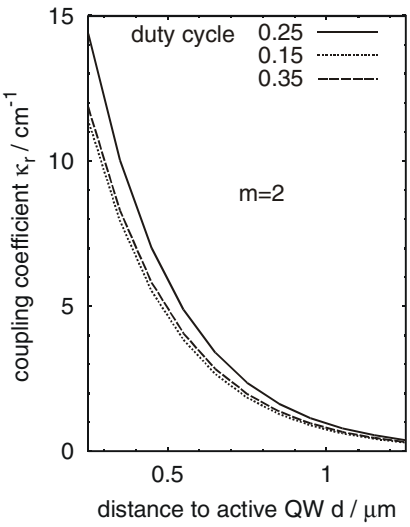

Figure 2. Calculated real part of the coupling coefficient of a second order rectangular-shaped index grating due to second order diffraction for TE polarization versus the distance *d* between grating and active QW (λ = 980 nm). Parameter is the duty cycle of the grating.

2. BASIC STRUCTURE AND FABRICATION

DFB lasers can be fabricated either in single or multiple growth steps. Single-growth devices use laterally coupled gratings. However, high-power fundamental-lateral mode operation of laterally coupled DFB lasers has not yet been demonstrated . Therefore, the Bragg grating has to be integrated into the epitaxial layer structure which requires a two-step epitaxy.

For lasers emitting in the desired wavelength region, AlGaAs or InGaAsP heterostructures can be employed. Owing to the high affinity of aluminum to oxygen, an Al-containing surface exposed to air can hardly be overgrown in a conventional metal-organic vapor phase epitaxy (MOVPE) reactor which complicates the fabrication of a Bragg grating integrated into the layer structure. On the other hand, the growth of AlGaAs is well established. For these reasons, AlGaAs is employed for the waveguide and cladding layers of the DFB lasers investigated. The Bragg grating is formed in an Al-free layer sequence of InGaP/GaAsP/InGaP embedded into the p-cladding layer.

Hence, the growth of the layer structure schematically drawn in Figure 1 and the fabrication of the Bragg grating takes place as follows. The first growth step consists of a n-GaAs buffer, n-AlGaAs cladding, 250 nm n-AlGaAs waveguide, the active layer, 250 nm p-AlGaAs waveguide, the first part of the p-AlGaAs cladding and the InGaP/GaAsP/InGaP layer sequence. The Bragg grating is formed in this layer sequence by holographic photolithography and wet-chemical etching. A frequency quadrupled Nd:YAG laser with an emission wavelength of λ = 266 nm is used in the holographic setup. It allows the fabrication of gratings with periods between 130 and 300 nm. In the second step the remainder of the p-AlGaAs cladding and a p-GaAs contact layer are grown. The active layer consists either of a tensile-strained GaAsP single quantum well (SQW) for the wavelength range 760-810 nm or a compressively strained InGaAsP or InGaAs SQW sandwiched between GaAsP spacer layers for λ = 810-980 nm.

The action of the Bragg grating is mainly determined by the contrast in the refractive indices of the GaAsP layer and the surrounding AlGaAs. Hence, the coupling coefficient κ between the forward and backward propagating waves depends on the thickness and the composition of the GaAsP layer. Keeping these parameters fixed for a reproducible fabrication of the grating, κ can be easily adjusted by the distance *d* between the InGaP/GaAsP/InGaP layer sequence and the active layer.

SPIE Proceedings Volume 5594 -- Physics and Applications of Optoelectronic Devices, pp. 110-123, Dec. 2004

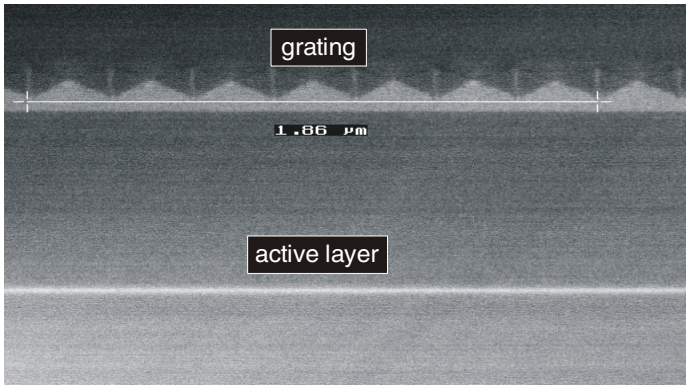

Figure 3. SEM picture of the cross section of the epitaxial layer structure showing the buried second order Bragg grating (top) and the active layer (bottom).

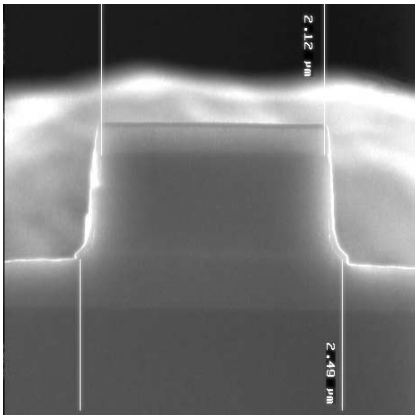

Figure 4. SEM picture of the cross section of the epitaxial layer structure showing the ridge waveguide.

In general, the complex coupling coefficient consists of several contributions [10]. The first contribution is due to the direct interaction (e.g., second order diffraction) with the index and loss grating and can be calculated for TE polarization according to the expression

$$\kappa = \frac{k_0^2}{2\Lambda\beta} \int_{\text{grating}} dx \int_0^{\Lambda} dz\, \varepsilon(x,z)\cos(m\frac{2\pi z}{\Lambda})E^2(x)\,, \qquad (1)$$

where k_0 is the free space wave vector, β the propagation constant and E the main electric field component of the reference waveguide, Λ the period and m the order of the grating, and ε the dielectric function. In case of a TM polarized mode, the expression has to be slightly modified. The second contribution is caused by the indirect interaction, where the radiation field excited by each guided wave affects the other one. This leads to an imaginary part of κ even for a pure index grating and a small correction of the real part of κ. The radiation increases also the internal losses for the guided waves. In our case of an index grating, the real part of Equation (1) denoted by κ_r in the following is the dominant contribution. The imaginary part κ_i mainly caused by the indirect interaction is much smaller than κ_r.

In Figure 2, κ_r of a second-order rectangular-shaped grating ($m = 2$) is plotted versus d. For the thickness (10 nm) and composition ($y = 0.15$) for the $GaAs_{1-y}P_y$ layer chosen, κ_r can be varied between 0.5 and 15 cm^{-1}. For a second-order rectangular-shaped grating, the duty cycle of the Bragg grating, given by the ratio Λ_1/Λ (compare Figure 8), must be carefully adjusted to the value 0.25 (or alternatively 0.75) because near $\Lambda_1/\Lambda = 0.5$ κ_r vanishes. For a first-order grating where κ_r is maximum at $\Lambda_1/\Lambda = 0.5$ the constraint on the duty cycle is less stringent.

The distance d to the active region should be as large as possible to reduce the impact of the critical interface between first and second growth on the electrical behavior, e.g. leakage currents. It should be mentioned, that the dependence of κ_r on d differs for the TM mode or for first order gratings.

The scanning electron microscope (SEM) micrograph in Figure 3 shows the epitaxial layer structure with the overgrown second order Bragg grating and the active layer. Lateral optical confinement is provided by a 2-3 µm wide, dry-etched ridge-waveguide (RW) with an effective-index step of $\Delta n_{eff} = 0.005$. A corresponding cross-sectional SEM picture is shown in Figure 4. The overall device structure and fabrication procedure is similar to that of the FP RW lasers described in Ref. [11]. After processing, the wafers were cleaved into bars with lasers having a cavity length of $L = 1.5$ mm. Then the front and rear facets were anti- and high-reflection coated, respectively, and the bars were cleaved into single laser chips. At the front facets, the reflection coefficients are typically of the order 10^{-4}. For continuous wave (CW) measurements, the chips were mounted p-up on AlN submounts and attached to copper heatsinks.

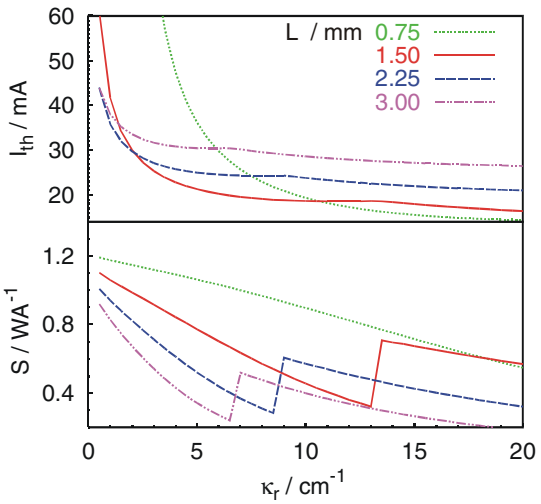

Figure 5. Calculated threshold current (top) and front facet slope efficiency (bottom) of a second order RW DFB laser versus the real part of the coupling coefficient κ ($\lambda = 980$ nm). Parameter is the cavity length. The imaginary part of κ and the internal losses were varied, too (see text). The front and rear facet reflectivities are $R_f = 0$ and $R_r = 0.95$.

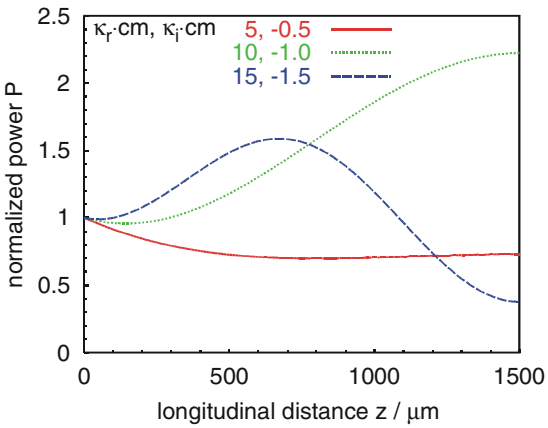

Figure 6. Longitudinal power profiles at threshold for different parameter sets around the jump of the slope efficiency in Figure 5 for L = 1.5 mm.

3. MODELLING

In order to simulate the RW DFB lasers, the coupled wave equations together with the transverse waveguide and carrier transport equations were solved according to the scheme presented in Ref. [12]. The optical gain and refractive index change in the active QW were calculated using a 8x8 **kp** method. The result of these simulations is the dependence of output power, wavelengths of lasing and nonlasing modes, sidemode suppression ratio and other laser parameters on the injection current. The optical spectrum below threshold can be also simulated.

Figure 5 shows the threshold current I_{th} and the slope efficiency S of a TE-emitting ridge-waveguide (RW) DFB laser as a function of the real part of κ for different cavity lengths L. The imaginary part of κ is varied phenomenologically according to $\kappa_i = -\kappa_r/10$ and the internal losses according to $\alpha_i = 4\ \text{cm}^{-1} - 2\kappa_i$. This variation is motivated by modeling results as well as parameter-extraction results using subthreshold optical spectra. The ridge width is W = 2.2 µm and the effective index step about $\Delta n_{eff} = 0.004$. The Bragg grating is of second order.

For high power operation, a large slope efficiency is needed. This can be achieved by decreasing κ_r or L. However, this is coupled with an increase of the threshold current (compare upper part of Figure 5) which degrades the thermal behavior. Therefore, a compromise for κ_r and L must be found in order to ensure a large slope efficiency and a moderately increased threshold current. For a better heat removal and lateral-mode stability, larger cavity lengths are in general to be preferred, for example $L = 1.5$ mm. For this length a κ_r value around 5 cm^{-1} is desired. According to Figure **2**, this leads to a distance $d \approx 600$ nm between the grating and the active QW.

The discontinuities in the plot of the front facet slope efficiency versus κ_r (Figure 5) are related to a hop of the lasing mode from the long- to the short-wavelength side of the stopband and are caused by the increased modulus of κ_r. The efficiency changes abruptly because the intra-cavity power profiles of the short and long wavelength modes differ; compare Figure 6. Increasing κ_r from 5 cm^{-1} to 10 cm^{-1} leads to a shift of the maximum of the power profile from the front to the rear facet. However, for $\kappa_r = 15$ cm^{-1} the maximum is again closer to the front facet because of the mode hop which leads to the enhanced slope efficiency.

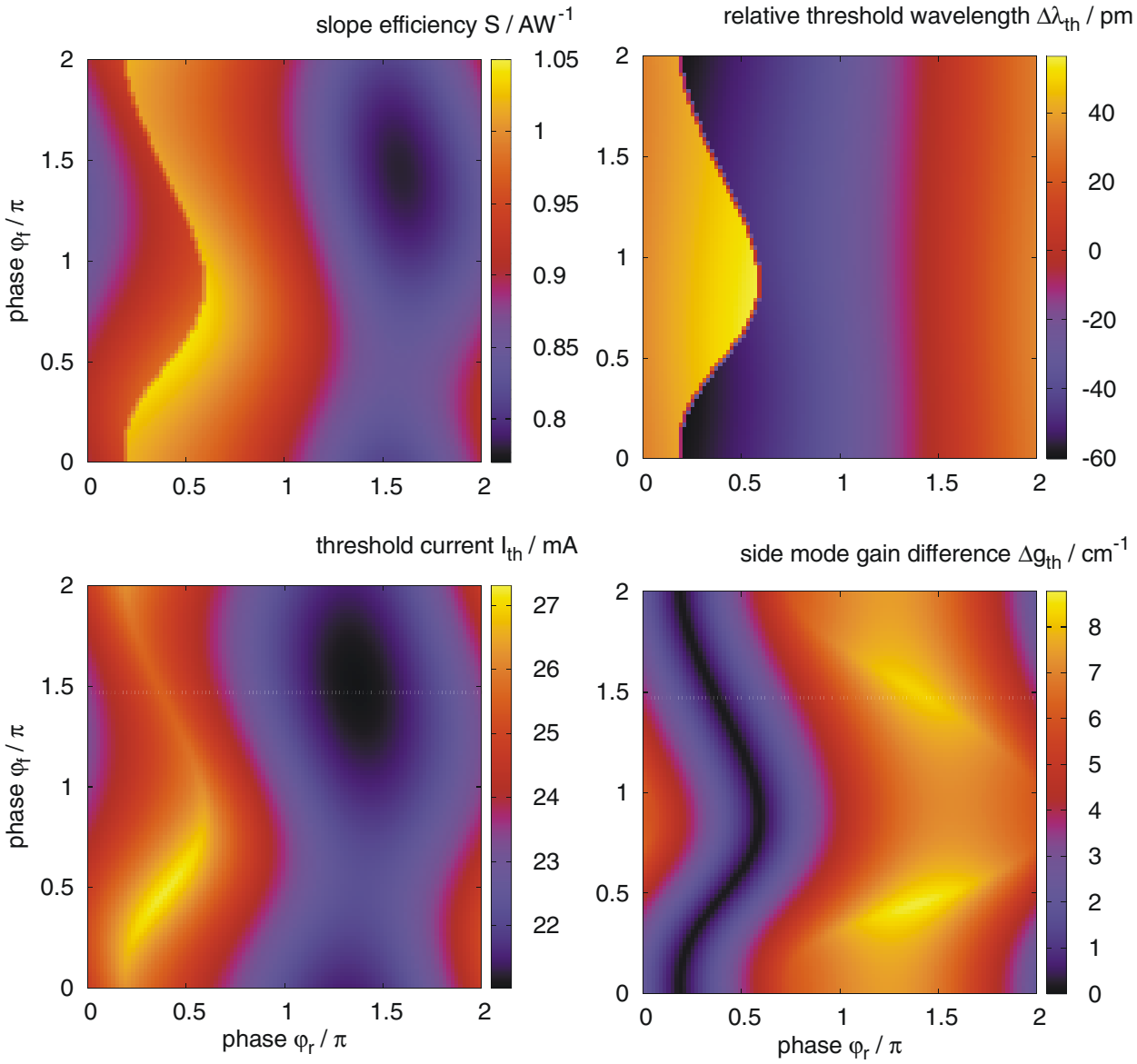

Figure 7. Calculated gray (color) scale plots of the slope efficiency (top left), relative threshold wavelength (top right), wavelength of the side mode relative to that of the lasing mode (bottom left) and threshold gain of the side mode relative to that of the lasing mode (bottom right) versus the phases of the grating at the facets for a second order Bragg grating with $\kappa_r = 5$ cm, $\kappa_i = -0.5$cm, $R_f = 10^{-3}$, $R_r = 0.95$, $\alpha_i = 5$ cm^{-1} and $L = 1.5$ mm ($\lambda = 860$ nm).

A similar mode hop and abrupt change of the slope efficiency occurs if the random phase φ_r of the grating at the rear facet is varied as shown in Figure 7. The grating phase is defined in Figure 8. Figure 7 shows as an example the results for $\lambda = 860$ nm. The observed behavior at other wavelengths is the same. From Figure 7 (top left) it can be concluded, that the slope efficiency S can vary by ±10% due to a variation of the phases of the grating. The phase at the rear facet has a larger influence because of the large reflectivity there. The threshold current I_{th} (Figure 7, bottom left) varies very similar to the slope efficiency, i.e. large values of S are linked with large values of I_{th}. An experimental verification of these findings is given in Figure 10 and Figure 11.

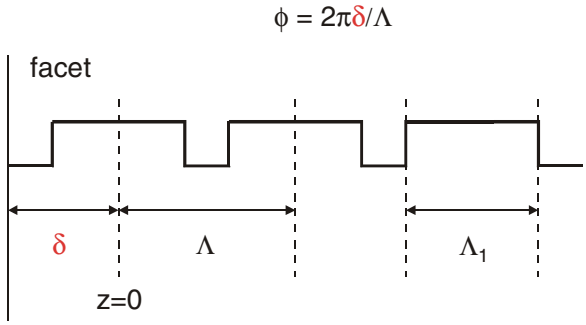

Figure 8. Definition of grating phase at the front facet (similar at the rear facet).

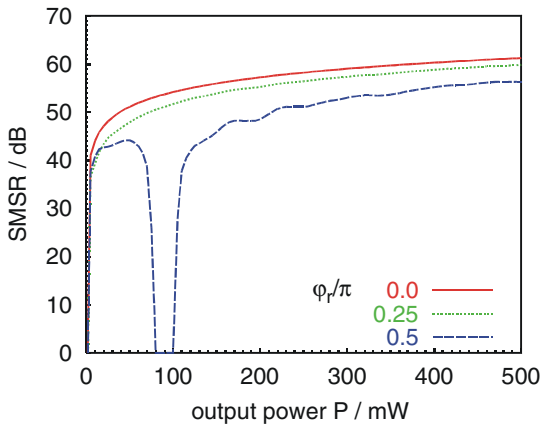

Figure 9. Calculated side mode suppression ratio versus output power for different grating phases at the rear facet. The phase at the front facet is $\varphi_f = 1.5\pi$ .The other parameters are the same as in Figure 7.

According to Figure 7 (top right), the lasing mode can be on the short- or long wavelength side of the stopband or even in the middle ($\Delta\lambda_{th} = 0$). There is a discontinuity for $\Delta\lambda_{th}$ around $\varphi_r = \pi/4$ (the exact value depends on φ_f) where the difference between the threshold gains Δg_{th} of the mode on either side of the stopband vanish (Figure 7, bottom right). However, this does not necessarily result in a poor mode stability above threshold as revealed by a calculation of the side mode suppression ratio (SMSR) following Ref. [12]. Figure 9 shows that instead for slightly larger values of φ_r the SMSR deteriorates at a certain output power and stabilizes again at higher output powers. The reason for this mode instability is longitudinal spatial holeburning. It should be mentioned, that the self-heating of the device, i.e. thermal effects, were not accounted for in these simulations.

The results concerning optimum cavity lengths and coupling coefficients for first-order gratings are very similar to those of second-order gratings, except that the discontinuities in Figure 5 are absent because the imaginary part of κ can be set to zero for an index grating. However, the dependencies of slope efficiency, lasing wavelength etc. on the phases of the grating as shown in Figure 7 are almost the same.

4. EXPERIMENTAL RESULTS

In the following experimental results of RW DFB lasers will be presented. In the wavelength range 850–980 nm devices with TE-polarized emission are studied while for λ = 760-790 nm TM polarization is used.

4. 1. TE-emitting RW DFB lasers

In Section 3 it was found by simulation, that the phase of the grating at the facets (especially the phase at the high-reflection coated rear facet) influences the slope efficiency and other laser parameters. The grating phases vary from laser bar to laser bar due to the limited precision of the cleavage. Furthermore, the grating grooves could be disoriented with respect to the facet, which would result in a variation of the phases of the grating along the laser bar from chip to chip.

Figure 10 depicts threshold current I_{th} and slope efficiency S versus the position of the corresponding laser on a bar. A modulation of both I_{th} and S can be clearly seen. The period of the modulation is between 4 and 5 positions. In order to understand the origin of this modulation, subthreshold optical spectra were measured. With a parameterized theoretical model for the amplified spontaneous emission (ASE) and an optimization routine as outlined in Ref. [13], the coupling coefficient, the phases of the grating at the facets and other parameters were extracted. In Figure 11 the determined phases are plotted against the position of the corresponding lasers on the bar. It can be clearly seen that the modulation period in Figure 11 is exactly the same as in Figure 10. The phase φ_r is modulated between 0 and 2π. The smaller modulation amplitude of phase φ_f can be attributed to a partial compensation of its impact by a variation of other parameters, e.g., the phase of the coupling coefficient.

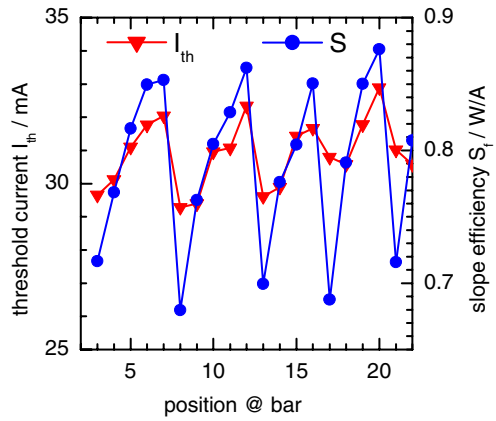

Figure 10. Measured threshold current (triangles, left axis) and slope efficiency (bullets, right axis) versus the position of the lasers at the bar (second order grating, λ = 855 nm).

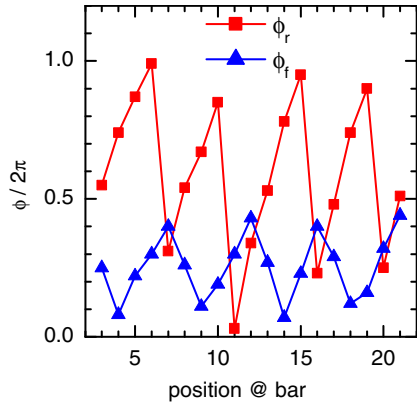

Figure 11. Phase of the grating at the front (triangles) and rear (squares) facets extracted from the subthreshold ASE spectra versus the position of the lasers at the bar. These are the same devices as in Figure 10.

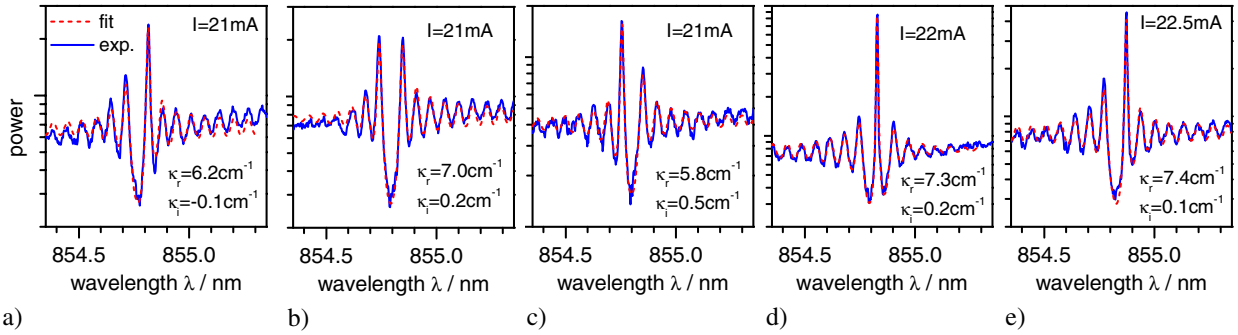

Figure 12. Experimental (solid) and fitted (dashed) subthreshold optical spectra of lasers at positions 11 (a), 12 (b), 13 (c), 14 (d) and 15 (e) at the bar. The injection current where the spectra were measured and the extracted real and imaginary parts of the coupling coefficients are indicated in the figures. These are the same devices as in Figure 10.

Figure 12 shows the measured and fitted spectra of the lasers at positions 11 to 15. The effect of the changing phases on the spectra can be clearly seen. The dominant mode of the lasers at positions 11 (a) and 15 (e) is on the long-wavelength side of the stopband and that of laser 13 (c) on the short-wavelength side. For laser 12 (b), both modes have nearly the same intensity, and for laser 14 (d), the dominant mode is located nearly in the middle of the stopband. Note the good agreement between the measured and fitted spectra. The extracted coupling coefficients are indicated in the figures, too. The real and imaginary parts of κ averaged over all 19 lasers are $\kappa_r = (7.0\pm0.8)$ cm^{-1} and $\kappa_i = (0.1\pm0.3)$ cm^{-1}, respectively. The large variation of the imaginary part can be attributed to the too small variation of the phase φ_f .

Figure 13 and Figure 14 show the light-current characteristic, the lateral farfield profile (inset) and a mapping of the optical spectrum of a RW DFB laser emitting around 860 nm. This type of laser has been successfully employed in a blue laser light source by passing the infrared laser beam through a potassium niobate ($KNbO_3$) crystal in a non-critical phase-matching arrangement to generate the second harmonic [14]. 120 mW input power at λ = 860 nm was converted to 1 mW output power at λ = 430 nm with low intensity noise and a high pointing stability ideally suited for digital film exposure systems.

The threshold current of the laser is about 32 mA, and the slope efficiency, for $P < 200$ mW, is as high as 0.9 W/A. The real part of the coupling coefficient determined by a fitting of the subthreshold optical spectrum is about 5 cm^{-1}. A maximum output power of almost 400 mW without any kink in the light-current characteristic has been achieved. The nearly Gaussian shape of the lateral farfield profile measured at I = 500 mA (P =350 mW) with a full width at half

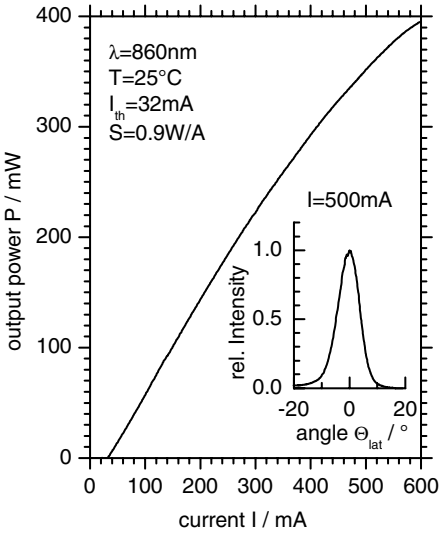

Figure 13. CW light-current characteristic of a second order 860-nm DFB laser. Inset: Normalized lateral far field profile at an injection current of 500 mA. Cavity length L = 1.5 mm.

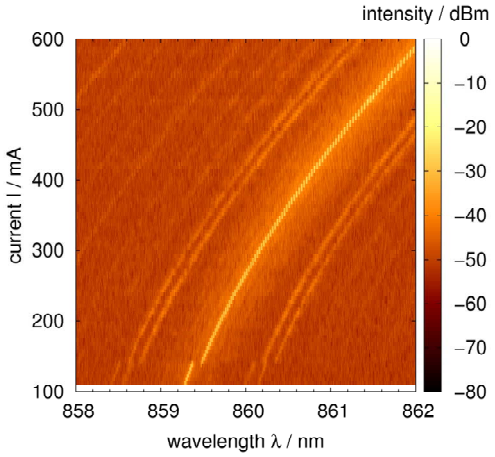

Figure 14. Color-scale plot of the optical spectrum of the device of **Figure 13** recorded with OSA Advantest Q8347.

maximum (FWHM) of about 9° indicates stable fundamental lateral mode operation. The FWHM of the vertical farfield profile (not shown) is about 22°. The mapping of the optical spectrum (Figure 14) reveals mode-hop free operation over more than 300 mW. The side peaks to be seen at the left and right hand side of the lasing mode are caused by the optical spectrum analyzer (OSA) used. The non-linear increase of the lasing wavelength seen in Figure 14 is mainly caused by the temperature induced change of the refractive indices due to Joule heating. From the wavelength variation of about $\Delta\lambda = 2.8$ nm between 100 and 600 mA a temperature rise of $\Delta T = 41$ K can be deduced on the basis of a temperature coefficient of $\Delta\lambda/\Delta T$=0.0675 nm/K determined near threshold.

Figure 14 also shows a mode hop around 140 mA where the lasing mode migrates from the short- to the long-wavelength side of the stop-band. This is more clearly seen in Figure 15 where the optical spectra measured at currents

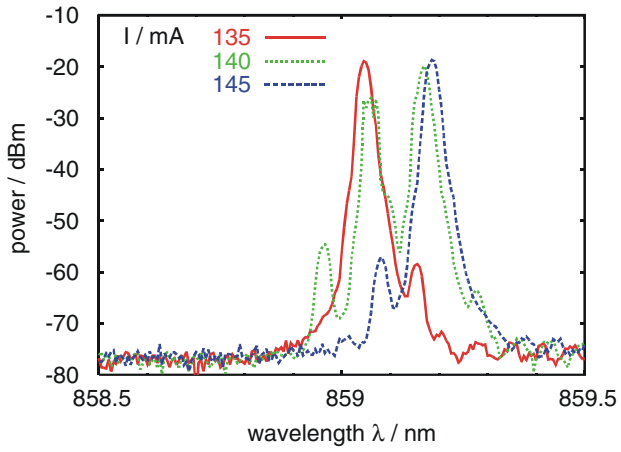

Figure 15. Optical spectra around the mode hop in Figure 14 recorded with the OSA Advantest Q8384. Parameter is the injection current.

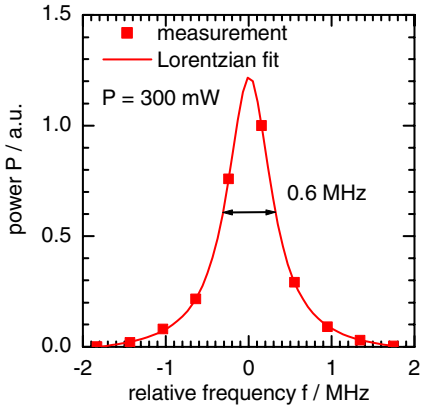

Figure 16. Spectral shape of the lasermode of the device of **Figure 13** at an output power of 300 mW recorded with a fiber interferometer.

around the instability are plotted. At $I = 140$ mA, both modes lase simultaneously and the corresponding four-wave mixing signals (small peaks) on either side can be observed. One should mention, that this mode hope does not lead to a corresponding kink in the PI characteristic measured at the front facet.

In order to determine the spectral linewidth of the lasing mode, the laser frequency fluctuations were measured using a homodyne fiber interferometer of Mach-Zehnder type with phase quadrature [15]. The laser was driven using a stabilized electrical power supply with current control. The resulting optical spectrum at an output power of 300 mW is shown in Figure 16. A Lorentzian fit of the experimental data yields a spectral linewidth as narrow as 600 kHz which belongs to the smallest values reported at this power level.

DFB lasers emitting at a wavelength of about 852 nm, the cesium D2 line, can be applied for the state selection in atomic clocks or for Doppler laser cooling. Figure 17 shows the light-current characteristics of such a laser measured between 20 and 40°C. The temperature dependence of threshold current and slope efficiency is very small. The lasing wavelength at a current of 300 mA and a heatsink temperature of 25°C is about 852.4 nm according to the optical spectrum depicted in the inset of Figure 17. The sidemode suppression ratio is larger than 50 dB.

If the laser beam is passed through a cesium vapor cell and the emission wavelength is tuned, the detected power should drop if the wavelength coincides with the D2 line and if the spectral linewidth is sufficiently small. The wavelength can be tuned either by a variation of the injection current or of the temperature of the heatsink of the laser. In Figure 18 light-current characteristics measured behind a cesium vapor cell are shown. The injection current where the power drop can be observed depends on the heatsink temperatures as expected. The modulation depth at the absorption line is larger than 15%.

Another wavelength region of particular interest is at around 980 nm. Lasers emitting at this wavelength are used as pump sources for erbium doped fiber amplifiers (EDFAs). Today's devices provide 500 mW in a single mode fiber. In order to increase the pump power to 1 W and above, several pump lasers can be combined using polarization and wavelength combiners. As the absorption window of erbium is less than 10 nm around 980 nm, the pumping wavelengths must be carefully chosen and stabilized. The use of DFB lasers instead of Fabry Perot lasers coupled to fiber Bragg gratings (FBGs) is one possible solution. DFB lasers offer also the possibility to integrate several frequency stabilized pump sources and erbium doped waveguides on a single chip without the need of aligning and fusing many FBGs. DFB lasers emitting at 976 nm can be also used as a replacement for certain argon ion lasers ($\lambda = 488$ nm) by frequency doubling using periodically poled $LiNbO_3$ or KTP crystals.

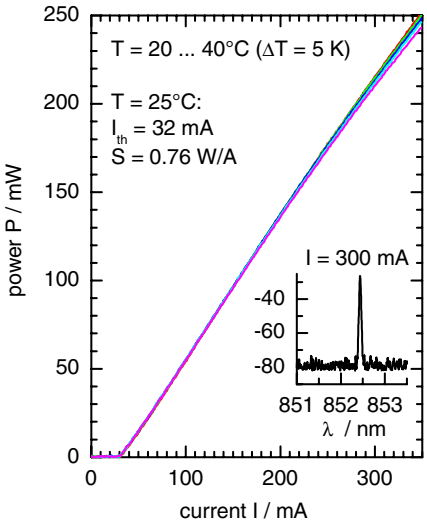

Figure 17. CW light-current characteristics of a second order 852-nm DFB laser for different heat sink temperatures. Inset: Optical spectrum recorded with OSA Advantest Q8384 at T = 25°C. Cavity length $L = 1.5$ mm.

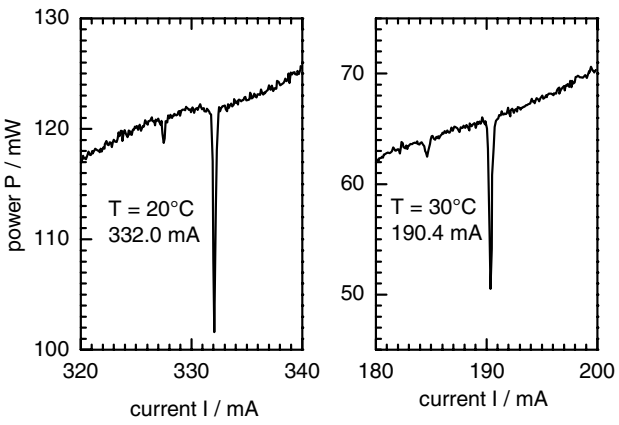

Figure 18. CW light-current characteristics of a second order 852-nm DFB laser measured after the passage of the emitted radiation through a cesium vapor cell for different temperatures of the laser heat sink.

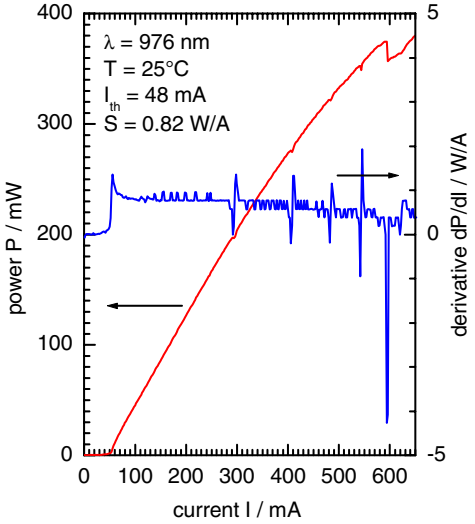

Figure 19. CW light-current characteristic (left axis) and its derivative (right axis) of a first order 976-nm DFB laser. Cavity length L = 1.5 mm.

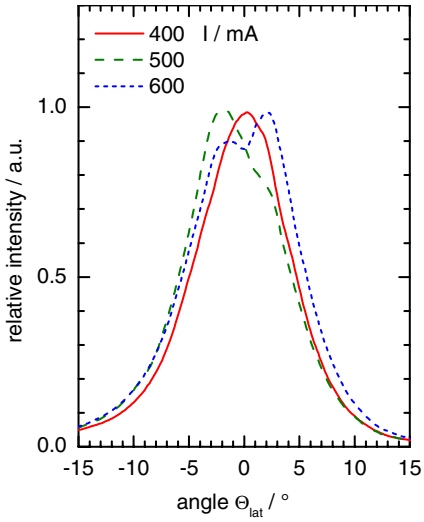

Figure 20. Normalized lateral farfield profiles of the device of Figure 19 for different injection currents.

Figure 19 shows the light-current characteristic and its derivative of a RW DFB laser with a first order grating emitting around 976 nm. An output power of almost 400 mW is achieved. The derivative of the P-I characteristic reveals several kinks. The first one is caused by the threshold and the last one at 590 mA by the appearance of the first order lateral mode (compare Figure 20). Below 500 mA the lateral farfield profiles depicted in Figure 20 demonstrate stable lasing of the fundamental lateral mode. One should mention that the beam steering observed at I = 500 mA is not related to a kink in the PI characteristic. Instead, the remaining 4 kinks are caused by absorption lines of water vapor present in the lab's air. Because the laser wavelength is tuned as the current is increased, the absorption spectrum of water vapor is scanned.

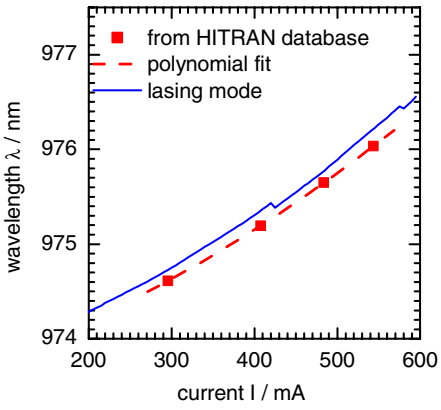

Figure 21. Lasing wavelength versus current obtained from the water vapor absorption lines in the HITRAN database (symbols and dashed line) and from the optical spectrum recorded with the OSA Advantest Q8384.

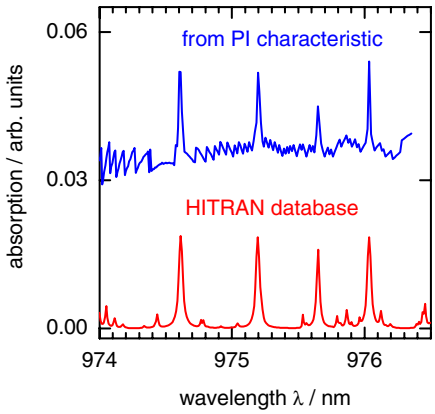

Figure 22. Absorbance obtained from the HITRAN database (lower graph) and light-current characteristic (upper). The upper graph was shifted by 0.03 for clarity.

This is demonstrated in Figure 21 where the wavelengths of 4 absorption lines extracted from the HITRAN database [16] together with the lasing wavelength taken from the measured optical spectrum are plotted versus current. Due to the inaccuracy of the OSA the measured wavelengths are slightly larger. However, the overall agreement is very good despite the fact that there are mode hops at 420 mA and at 580 mA. Whereas the first one is of the same type as discussed above (Figure 14), is the second one related to the corresponding kink in the P-I characteristic. Figure 22 shows the absorption spectra obtained from the HITRAN database and calculated from the P-I characteristic assuming an absorption length of 10 m which is estimated from the multiple reflections occurring in the integrating sphere used as detector.

The water vapor absorption is much stronger in the wavelength range between 930 and 955 nm. Hence, DFB lasers emitting in this wavelength range should exhibit deep drops in the light-current characteristics and should be ideally suited for the remote sensing of water vapor.

4. 2. TM-emitting RW DFB lasers

DFB lasers emitting in the wavelength range between 760 and 795 nm are of particular interest for applications in nonlinear frequency conversion, excitation of rubidium atoms (Rb87 D2 and D1 lines at 780 nm and 794 nm, respectively), oxygen absorption spectroscopy and Raman spectroscopy.

The active region of these lasers developed by our group consist of Al-free tensile-strained GaAsP SQWs which were proven to yield both high power [17] and highly reliable [18] broad area lasers. Owing to the large tensile strain, the laser operates steadily in the TM mode. Figure 23 shows the light-current characteristic and the optical spectrum recorded at P = 220 mW (inset) of a RW DFB laser emitting at 785 nm. The threshold current is as low as 29 mA and the slope efficiency, for P < 150 mW, is S = 0.85 W/A. This type of laser was successfully used as a light source in surface-enhanced Raman scattering (SERS) experiments [19].

The light-current characteristic of a DFB laser emitting around 763 nm depicted in Figure 24 exhibits a similar decrease in the detected output power as in Figure 19. However, the reason is now the absorption due to oxygen molecules. This is demonstrated in Figure 25 where the wavelengths of 4 absorption lines extracted from the HITRAN database [16] together with the lasing wavelength taken from the measured optical spectrum are plotted versus current. The corresponding absorption spectra obtained from the HITRAN database and calculated from the P-I characteristic are shown in Figure 26. It should be mentioned, that the first application of a GaAs/AlGaAs DFB laser to spectroscopic based oxygen sensing was reported in Ref. [20].

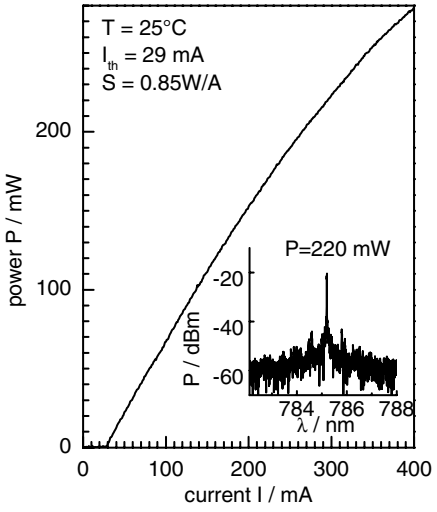

Figure 23. CW light-current characteristic of a second order 785-nm DFB laser. Inset: Optical spectrum recorded with OSA Advantest Q8347. Cavity length L = 1.5 mm.

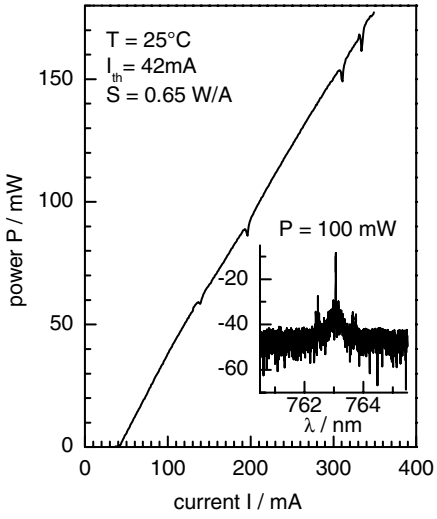

Figure 24. CW light-current characteristic of a second order 763-nm DFB laser. Inset: Optical spectrum recorded with OSA Advantest Q8347. Cavity length L = 1.5 mm.

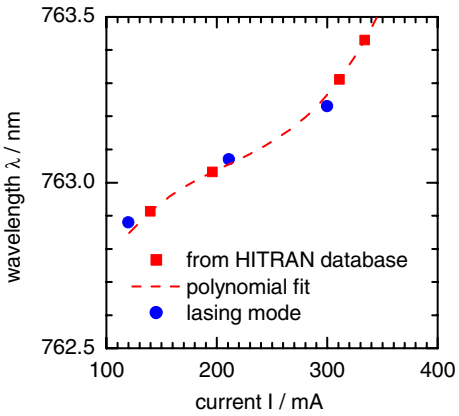

Figure 25. Lasing wavelength versus current obtained from the oxygen absorption lines in the HITRAN database (squares and dashed line) and from the optical spectrum recorded with the OSA Advantest Q8347 (bullets).

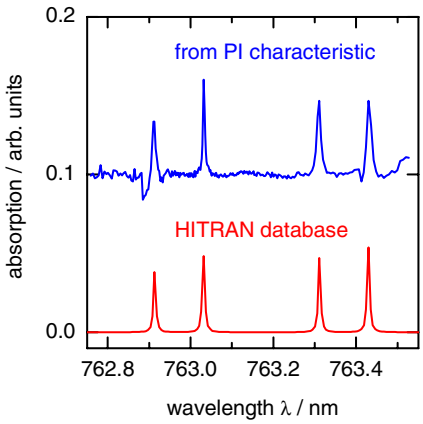

Figure 26. Absorbance obtained from the HITRAN database (lower graph) and light-current characteristic (upper). The upper graph was shifted by 0.1 for clarity.

4. 3. Lifetime tests

In order to investigate the reliability, 5 DFB lasers emitting at 860 nm were aged over 8000 h at a constant power of P = 250 mW and 5 DFB lasers emitting at 773 nm were aged over 2000 h at a constant power of P = 150 mW, both lots at room temperature. The results of the aging tests are shown in Figure 27 and Figure 28. The degradation rates are below 5×10^{-6}/h (Figure 27) and below 10^{-5}/h (Figure 28) obtained from a linear fit over the last 1000 h. Thus, it can be concluded that the Bragg grating integrated into the cavity does not the degrade the long-term reliability.

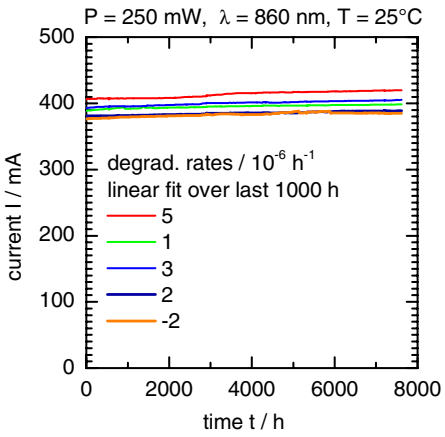

Figure 27. Aging test of 5 TE-emitting 860-nm lasers driven at a constant power of 250 mW at room temperature

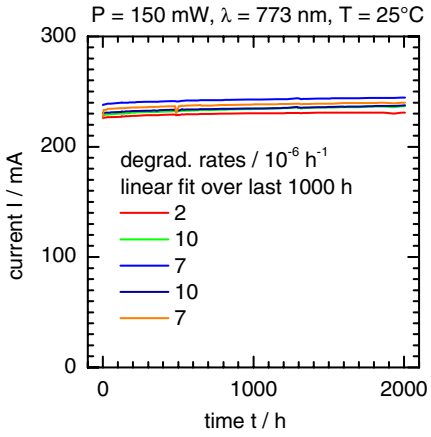

Figure 28.. Aging test of 5 TM-emitting 773-nm lasers driven at a constant power of 150 mW at room temperature.

SPIE Proceedings Volume 5594 -- Physics and Applications of Optoelectronic Devices, pp. 110-123, Dec. 2004

5. CONCLUSIONS

We have demonstrated singlemode single-frequency operation of RW DFB lasers emitting between 760 nm and 980 nm either in TM or TE polarization. A maximum continuous-wave output power of about 400 mW, spectral linewidth below 1 MHz and a side mode suppression ratio greater than 50 dB can be achieved at room temperature. TE and TM emitting DFB lasers are very similar in their performance. The measured light-current characteristics exhibits the expected decrease in intensity, if the lasing wavelength coincides with an absorption line of atoms or molecules present in the optical path. This has been demonstrated with water vapor, cesium vapor and oxygen.

ACKNOWLEDGMENTS

The authors are grateful to H. Götzelt, R. Selent and J. Hopp for technical assistance.

REFERENCES

1. A. Mathur, M. Ziary, V. Agrawal, E. Kolev: "High power 1.3µm DFB lasers", *Electronics Lett.* **34**, pp. 2334-2336, 1998.
2. R. Menna, A. Komissarov, M. Maiorov, V. Khalvin, A. Tsektou, S. Todorov, J. Connolly, D. Garbuzov: "High-power single spatial and longitudinal mode 1310 nm InGaAsP/InP lasers", *27th EOC Amsterdam*, TU.B.1.6, 2001
3. K. Inoguchi, H. Kudo, S. Sughara, S. Ito, H. Yagi, H. Takiguchi: "Operation of 780 nm AlGaAs distributed feedback lasers at 100°C with low-loss waveguide structure", *Jpn. J. Appl. Phys.* **33**, pp. 852-855, 1994.
4. N.A. Morris, J.C. Connolly, R.U. Martinelli, J.H. Abeles, A.L. Cook: "Single-mode-distributed-feedback 761-nm GaAs-AlGaAs quantum-well lasers", *IEEE Photonics Technol. Lett.* **7**, pp.455-457, 1995.
5. R.M. Lammert, J.E. Ungar, S.W. Oh, H. Qi, J.S. Chen: "High-power InGaAs-GaAs-AlGaAs distributed feedback lasers with nonabsorbing mirrors", *Electronics Lett.* **24**, pp. 886-887, 1998.
6. S. Okada, T. Fujimoto, Y. Yamada, A. Okubo, K. Muro: "High-power single longitudinal mode operation of distributed feedback laser diodes with a decoupled confinement heterostructure", *Review of Laser Engineering* **27**, pp. 484-492, 1999.
7. J.S. Major, S. O'Brian, V. Gulgazov, D.F. Welch, R.J. Lang: "High-power singlemode AlGaAs distributed Bragg reflector laser diodes operating at 856 nm", *Electronics Lett.* **30**, pp. 496-497, 1994.
8. H. Wenzel, A. Klehr, M. Braun, F. Bugge, G. Erbert, J. Fricke, A. Knauer, M. Weyers, G. Tränkle: "High-power 783 nm distributed-feedback laser", *Electronics Lett.* **40**, pp. 123-124, 2004.
9. H. Wenzel, M. Braun, J. Fricke, A. Klehr, A. Knauer, P. Ressel, G. Erbert, G. Tränkle: "High-power ridge-waveguide distributed-feedback lasers emitting at 860 nm", Electronics Lett. **38**, pp. 1676-1677, 2002.
10. A.M. Shams-Zadeh-Amiri, J. Hong, X. Li, W.-P. Huang: "Second – and Higher Order Resonant Gratings with Gain or Loss" *IEEE J. Quantum Electron.* **36,** pp. 1421-1437, 2000.
11. G. Beister, F. Bugge, G. Erbert, J. Maege, P. Ressel, J. Sebastian, A. Thies, and H. Wenzel: "Monomode emission at 350 mW and high reliability with InGaAs/AlGaAs (λ = 1020 nm) ridge waveguide laser diodes", *Electronics Lett.* **34**, pp. 778-77, 1998.
12. H.-J. Wünsche, U. Bandelow, H. Wenzel: "Calculation of combined lateral and longitudinal spatial hole burning in $\lambda/4$ shifted DFB lasers", *IEEE J. Quantum Electron.* **29**, pp. 1751-1760, 1993.
13. H. Wenzel: "Green's function based simulation of the optical spectrum of multisection lasers", *IEEE J. Select. Top. Quant. Electron.* **9**, pp. 865-871, 2003.
14. H.-J. Pätzold, J. Paetow: "Blue laser light source enhances computer-to-plate technology", *Europhotonics October/November 02*, pp. 31-33, 2002.
15. Th. Kinder, K.-D. Salewski: "Characterizing tuneable external cavity semiconductor lasers using a homodyne fibre interferometer", *Optik (Jena)* **111**, pp. 127-131, 2000.
16. L.S. Rothman; A. Barbe, D. Chris Benner, L.R. Brown, C. Camy-Peyret, M.R. Carleer , K. Chance, C. Clerbaux, V. Dana V.M. Devi, A. Fayt, J.-M. Flaud, R.R. Gamache, A. Goldman, D. Jacquemart, K.W. Jucks, W.J. Lafferty, J.-Y. Mandin, S.T. Massie, V. Nemtchinov, D.A. Newnham, A. Perrin, C.P. Rinsland, J. Schroeder, K.M. Smith, M.A.H. Smith, K. Tang, R.A. Toth, J. Vander Auwera, P. Varanasi, K. Yoshino: "The HITRAN molecular spectroscopic database: edition of 2000 including updates through 2001", *J. Quantitative Spectroscopy Radiative Transfer* **82**, pp. 5–44, 2003. Also available online from http://www.hitran.com/

17. G. Erbert, F. Bugge, A. Knauer, J. Sebastian, A. Thies, H. Wenzel, M. Weyers, G. Tränkle: "High-power tensile – strained GaAsP-AlGaAs quantum-well lasers emitting between 715 and 790 nm", *IEEE J. Select. Top. Quant. Electron.* **5**, pp. 780-784, 1999.
18. B. Sumpf, G. Beister, G. Erbert, J. Fricke, A. Knauer, W. Pittroff, P. Ressel, J. Sebastian, H. Wenzel, G. Tränkle: "2W reliable operation of λ = 735nm GaAsP/AlGaAs laser diodes", *Electronics Lett.* **37**, pp. 351-353, 2001.
19. H. Wenzel, A. Klehr, M. Braun, A. Knauer, B. Sumpf, G. Erbert, H. Schmidt, H.-D. Kronfeldt: "A distributed feedback diode laser and its application as a Raman light source", *Europhysics Conf. Abstracts CLEO Europe* **27E**, Paper CI5 05 WED, 2002.
20. V. Weldon, J. O'Gorman, J.J. Perez-Camacho an J. Hegarty: "Oxygen sensing using single frequency GaAs-AlGaAs DFB laser diodes and VCSELs", *Electronics Lett.* **32**, pp. 219-218, 1996.